Software and data availability

Software Name: A new coupled thermodynamic-based FMC and FDS model
Developers: Ritambhara Raj Dubey, Neda Yaghoobian
Contact information: rrd20z@fsu.edu, nyaghoobian@fsu.edu
Year first available: 2024
Program language: Fortran
Cost: Free
Software availability: https://github.com/ritambhara1234/Physics-Based-Dynamic-FMC
Program size: 7.5 MB
Data availability: Data archive can be found in following locations

- https://github.com/ritambhara1234/Physics-Based-Dynamic-FMC/tree/main/Input%20data/Dynamic%20FMC%20model for the new model validation
- https://github.com/ritambhara1234/Physics-Based-Dynamic-FMC/tree/main/Input%20data/Coupled%20FMC-FDS%20model for the Coupled FMC-FDS Model validations

Size of archive: 0.23 MB

A Physics-Based Model of Thermodynamically Varying Fuel Moisture Content for Fire Behavior Prediction

Ritambhara Raj Dubey, Neda Yaghoobian*

Florida State University, FAMU-FSU College of Engineering, Department of Mechanical Engineering, Tallahassee, FL, USA

*Corresponding email address: nyaghoobian@eng.famu.fsu.edu

Abstract

Fuel moisture content (FMC) is a critical parameter in fire and plume behaviors, showing diurnal and spatial variations influenced by local meteorological conditions, soil characteristics, and fuel properties. In low-intensity fires, small-scale FMC variations intensify, leading to an amplification of their effects on fire physics. In an effort to capture these variations, this paper presents the development of a physics-based model that couples a thermodynamic-based FMC prediction model for dead fuels with the Fire Dynamics Simulator of the National Institute of Standards and Technology. The model accuracy is validated against several existing experimental data, showing improvements over the baseline model which uses the kinetic-based Arrhenius drying approach. A case study of flame propagation in a small fuel bed is also presented, indicating the improved performance of the new model and its novel capabilities in capturing complex processes of fuel drying and moisture flux exchanges between the fuel and ambient atmosphere.

Keywords: Dead fuel; FDS; FMC; Fire behavior; Low-intensity fires; Plume dynamics, Thermodynamic approach

Introduction

Fuel moisture content (FMC), which is defined as the ratio of water in the fuel and the dry mass of the fuel, has a pivotal role in fire events: the fuel ignitability (Dimitrakopoulos et al., 2001; Fernandes et al., 2008), fire behavior (Asensio et al., 2023; Burrows, 1999; Pimont et al., 2019; Rothermel, 1972; Yebra et al., 2013), plume concentration and spread (Marcelli et al., 2004; Morvan, 2013; Potter, 2005), and fire severity are all impacted to varying degrees by the FMC. In the solid medium, the fuel moisture modifies the solids' thermal and physical properties (i.e., thermal conductivity, specific heat, and density) and affects their ignitability by altering the heat energy required to vaporize moisture (Simms & Law, 1967). As a result, the variation in fuel moisture regulates the local fire spread (Loudermilk et al., 2017; Marshall et al., 2023; Nelson Jr, 2001), heterogeneity of the burned areas (Parsons et al., 2017; Wu et al., 2018), and the fire intensity (Kane, 2021; Tanskanen et al., 2006). In the gas phase, the fuel moisture released by the drying and evaporation processes impacts the temperature and velocity distribution inside the plume (Marcelli et al., 2004), the temperature of the flame (Ferguson et al., 2013), and the emission of particulate matter (Robertson et al., 2014). Owing to its multifaceted effect on various aspects of fire, fuel moisture is an essential input to the fire danger indicators (e.g., Forest, 1984; Noble et al., 1980; Stocks et al., 1989) and fire-atmosphere interaction models (Coen, 2013; Filippi et al., 2018; R. Linn et al., 2002; R. R. Linn et al., 2020, p. 202; Mell et al., 2007; Skamarock & Klemp, 2008). Incorporating the information of FMC variations also enhances the wildfire occurrence probability predictions (Quan et al., 2024).

Wildland fuels are a mixture of live and dead fuels, both of which play crucial roles in determining fire behavior. The moisture content of live fuels changes slowly in response to the atmospheric conditions, while the dead fuel moisture content responds rapidly to the atmospheric conditions and thus experiences significant variations diurnally (Chuvieco et al., 2004). Recent studies developed models to predict Live Fuel Moisture Content (LFMC) using remote sensing data, utilizing optical and microwave data gathered by Earth-orbiting satellite sensors (Marino et al., 2020; Miller et al., 2023; Rao et al., 2020). These techniques provide live fuel moisture prediction over large areas at low to moderate resolutions, typically ranging from 0.5 to 5 km (Miller et al., 2023; Vinodkumar et al., 2021).

The dead FMC is influenced by the vegetation characteristics, soil conditions, and the phenological and micro-meteorological conditions at the local scale (Clements et al., 2015; Iván et al., 2023; Wiesner et al., 2019), adding additional elements of complexity to the fuel representation (Hiers et al., 2020; Pimont et al., 2016). As the temporal variation of dead fuel moisture significantly influences fire and plume behavior, numerous efforts have been made to model this variability. Methodologies to estimate the dead FMC are broadly classified into empirical and physics-based modeling techniques. The former approach involves setting up statistical correlations between the fuel moisture and atmospheric conditions derived from laboratory-based (Byram et al., 2015; E. A. Catchpole et al., 2001; Nelson Jr, 1984) or field-based experiments (Alves et al., 2009; Ferguson et al., 2002; Lin, 2004; Ray et al., 2010; Sharples et al., 2009). In recent studies, data from these traditional approaches have been used to train machine learning-based fuel moisture prediction models (e.g., Fan et al., 2023; Hou et al., 2024). The empirical-based models provide fuel-specific, ambient condition-dependent FMC prediction and thus, cannot be easily adapted universally. Physics-based models, however, are universal as they are developed based on the physical laws governing the FMC variation and provide an explicit relationship between the atmospheric conditions, soil conditions, fuel properties, and FMC. To the best of our knowledge, only two physics-based FMC prediction models for dead fuels are currently available: Wittich (2005) developed a fine fuel moisture prediction model that simulates heat and moisture transport inside fine fuels. In this model, the rate of change of moisture varies with the precipitation, drainage, absorption, and evaporation rate of water. Two identified limitations (Matthews, 2014; Wittich, 2005) of this model are that the heat and water transfer between the litter layers and the underlying soil is not considered, and the model has not been tested for a forest environment whose microclimate differs from that of an open grass field (due to the interception of rain and radiation by trees). Forest canopies play important roles in the amount of FMC and its variations over time by influencing the precipitation intensity and its duration (Diószegi et al., 2023). These limitations are addressed in the physics-based fuel moisture prediction model of Matthews (2006), which represents the transfer of energy and water in the fuel bed and considers the thermodynamic interaction of FMC with the soil and atmosphere. The model also predicts changes in the fuel moisture due to the varying local solar radiation, ambient temperature, relative humidity, wind speed, and rainfall.

There are two primary methods for physics-based modeling of moisture evaporation in forest fuels within fire-atmosphere interaction models. The first is the heat sink approach, which assumes that evaporation occurs at the boiling temperature of water. This method treats evaporation as primarily controlled by heat transfer, with the assumption that there is no resistance to the water vapor mass transfer. The second method is the Arrhenius approach, which considers evaporation as a kinetic process. The kinetic approach provides information on how fast evaporation can occur by determining the rate of drying. It describes evaporation using a set of kinetic parameters (e.g., pre-exponential factor and activation energy) and fuel temperature. While the kinetic approach provides insights into the rate of evaporation, it has some known limitations. Firstly, obtaining a unique set of kinetic parameters for different fuels is challenging. Additionally, the Arrhenius model struggles to capture the characteristics of high-temperature or high-heating rate drying scenarios, such as large gradients in liquid moisture, and it inaccurately predicts low-temperature drying behaviors (Borujerdi et al., 2019).

A third approach, not currently utilized in the fire-atmospheric interaction models, is the thermodynamic approach. This method focuses on the phase change nature of moisture evaporation, considering that the liquid water and vapor coexist in thermodynamic equilibrium. The thermodynamic approach models fuel drying as a complex process influenced by the water vapor mass fraction and temperature gradients between the porous fuel layers, and the fuel and its surroundings. Previous studies indicated that the thermodynamic approach represents the underlying physics of evaporation more accurately in comparison with the Arrhenius method (Borujerdi et al., 2019).

In fire behavior modeling, the choice of evaporation modeling approaches impacts the accuracy of fire and smoke behavior predictions, especially in scenarios involving low-intensity fires. In these cases, the finer-scale variations within the fire environment become more noticeable, underscoring the need for precise modeling (Jonko et al., 2021; R. R. Linn et al., 2021; Marshall et al., 2023). In these scenarios, the presence of significant temperature variations within both solid materials and the surrounding environment plays a crucial role in influencing drying and pyrolysis processes, consequently affecting the behavior of fire spread (Marshall et al., 2023). As communities increasingly recognize the importance of low-intensity prescribed fires as essential ecological processes that can enhance natural resources and human health (Hiers et al., 2020), the accurate depiction of these fires becomes imperative.

The study in the current paper aims to develop a new modeling capability for investigating the role of the spatiotemporal variations of dead fuel moisture content on local fire behavior and plume dynamics using the thermodynamic approach. To this end, the physics-based fuel moisture prediction model of Matthews (2006) is coupled with the Fire Dynamics Simulator (FDS; McGrattan et al., 2004) developed by the National Institute of Standards and Technology (NIST). For the development of the model, the most recent version (v6.8.0) of FDS was employed. In the following, we first explain the two models (i.e., Matthews FMC model and FDS) and their coupling. This is followed by a description of validation studies of the FMC model and the two-way coupled model. We also briefly discuss a study of flame propagation in a laboratory-size pine needle fuel bed using the coupled model, followed by a summary section. In addition, we provide our exploratory validation studies of the baseline FDS model in the Appendix Section for scenarios of flows over topographies and in daytime atmospheric boundary layer as an additional resource to the FDS users.

Model Description

Fire Dynamics Simulator (FDS)

FDS is a physics-based computational fluid dynamics fire-atmosphere interaction model. It solves the three-dimensional (3D) filtered continuity, momentum, species transport, enthalpy, and ideal gas equations using the large-eddy simulation (LES) technique for low Mach number ($<$ 0.3) flows to obtain flow velocity, hydrodynamic pressure, temperature, species mass fraction, and species density (McGrattan et al., 2004). In the LES technique of FDS (McDermott, 2005), the turbulent motions larger than the filter size are resolved directly while the smaller eddies are modeled using a turbulent closure scheme based on the Deardorff's model (Deardorff, 1980), in which the turbulent viscosity is a function of sub-grid scale turbulent kinetic energy (TKE). The sub-grid scale TKE is determined from the resolved velocity field using an algebraic scale similarity approach (Bardina et al., 1980). To appropriately scale the eddy viscosity near the wall, the wall adapting local-eddy (WALE) model is used in the first grid cell next to the wall, wherein the eddy viscosity is determined by the filtered density, LES filter width, model constant (C_w), and a combination of strain rate and rotation rate tensor. The default model constant value of $C_w = 0.6$ was used for the current study. The low Mach number assumption helps to eliminate the need for solving the energy equation explicitly and speeds up the simulations, while the hydrodynamic solver guarantees that the energy equation is satisfied at each time step. More details of the FDS model can be found in McGrattan et al. (2004).

In the following, we first describe how the fuel temperature is calculated in FDS, to explain the heat sink and Arrhenius FMC models within FDS and later, the coupling of the new thermodynamic-based FMC model and FDS. Fire propagation in FDS can be modeled using either a semi-empirical method (based on a level-set scheme) or a physics-based approach. In the physics-based method, the fuel is represented either by fixed lagrangian particles that act as sources of drag, heat, and mass fluxes or by a boundary-fuel method. The bulk influence of the drag force in the gas phase momentum depends on the fuel physical properties (i.e., density, surface area to volume ratio, packing ratio, and shape factor), the local velocity of the flow, and the local Reynolds number. The net heat flux due to the fire convection and radiation at the bottom boundary of the gas cells alters the temperature of the solid fuel. The temperature evolution of a solid fuel (T_s (K)) with time (t (s)) in FDS is, therefore, found using Eq. (1):

$$\rho_s c_{p,s} \frac{\partial T_s}{\partial t} = -\Delta h_{vap} R_{H_2O} - \Delta h_{pyr} R_{pyr} - \alpha_{char} \Delta h_{char} R_{char} + \dot{q}_{s,c}''' + \dot{q}_{s,r}''' \tag{1}$$

In this equation, $\rho_s c_{p,s}$ is the volumetric-averaged heat capacity of the fuel, with ρ_s (kg m^{-3}) and $c_{p,s}$ (J kg^{-1}K^{-1}), respectively, being the solid fuel density and specific heat. Δh_{vap} (J kg^{-1}), Δh_{pyr} (J kg^{-1}), and Δh_{char} (J kg^{-1}) are the heat of vaporization, heat of pyrolysis, and heat of char oxidation, and R_{H_2O} (kg m^{-3}s^{-1}), R_{pyr} (kg m^{-3}s^{-1}), and R_{char} (kg m^{-3}s^{-1}) are the reaction rates for evaporation, pyrolysis of dry vegetation, and char oxidation, respectively. α_{char} represents the fraction of heat generated due to the char oxidation reaction, and $\dot{q}_{s,c}'''$ (W m^{-3}) and $\dot{q}_{s,r}'''$ (W m^{-3}) are the fire heat flux due to convection and radiation, respectively. The averaged properties of the fuel depend on the volume fraction of components in the fuel (i.e., water, dry solid fuel, and char) and are influenced by both the dry fuel and FMC.

In FDS, the FMC can be treated using one of the two following approaches. The first, which is based on the heat sink approach, assumes FMC is constant everywhere and is defined by a single user-defined value. In this approach, when the temperature of the solid fuel (T_s) exceeds the boiling point of water (100°C), all the heat energy supplied to the fuel is used to evaporate the fuel moisture. The second approach considers that fuel moisture decays with increase in fuel temperature following the Arrhenius drying equation. The Arrhenius equation describes the temperature dependence of evaporation rate, treating fuel drying as a kinetic process that converts liquid to water vapor (Borujerdi et al., 2019). The rate of reaction for evaporation using the

Arrhenius equation (Eq. 2) is dependent on the water vapor density in the fuel ρ_{s,H_2O} (kg m^{-3}), pre-exponential factor A_{H_2O} (K$^{1/2}$ s^{-1}), activation energy E_{H_2O} (K), and fuel temperature. As it is evident from this equation, the evaporation rate depends on the thermo-kinetic constants A_{H_2O} and E_{H_2O}, and it's worth noting that these constants vary depending on the type of fuel (Grishin et al., 2003).

$$R_{H_2O} = \rho_{s,H_2O}\, A_{H_2O}\, T_s^{-0.5}\, e^{-E_{H_2O}/T_s} \tag{2}$$

Following either of these approaches for estimating FMC, the solid fuel decomposes according to a two-stage endothermic process: evaporation of fuel moisture accompanied by volatilization of the solid fuel. These processes result in a change in density of water vapor in the fuel (through Eq. 3), and mass loss of the fuel, which modifies the fuel density (through Eq. 4) and the gas phase density, species, and enthalpy equations.

$$\frac{\partial \rho_{s,H_2O}}{\partial t} = -R_{H_2O} \tag{3}$$

$$\frac{\partial \rho_s}{\partial t} = -R_{H_2O} - (1 - \chi_{char})R_{pyr} - (1 - \chi_{ash})R_{char} \tag{4}$$

In Eq. (4) χ_{char} and χ_{ash} are, respectively, the fraction of dry fuel converted to char and the fraction of char converted to ash.

Thermodynamic-based FMC prediction model

In this paper, the temporal variation in the FMC is modeled by employing the physics-based FMC variation model of Matthews (2006). The model represents the transfer of energy and liquid water and their two-way interactions in a fuel bed that is bound between the atmosphere and soil. The fuel bed is composed of multiple layers, each consisting of three components: solid fuel, air, and free liquid water. The model is governed by the local ambient conditions (i.e., precipitation, diurnal solar radiation, relative humidity, wind speed, and air temperature), and the physical (e.g., surface area to volume ratio, packing ratio, and height of the fuel bed) and thermal (i.e., specific heat and thermal conductivity) properties of the fuel. In the following, the process of fuel drying and the heat and moisture exchanges in fuel layers are explained.

When the fuel dries, the fuel moisture undergoes phase change from liquid water (in the solid and liquid components of fuel) to water vapor and is transferred to the fuel air spaces. The flux of water vapor from solid to air spaces and the evaporation of liquid water to air spaces are, respectively, represented by the flux terms E_{ma} (Eq. 5) and E_{la} (Eq. 6). It should be noted that, in describing Matthews (2006) model in the following equations, subscripts m, a, and l, are respectively related to solid, air, and liquid components of the fuel. In Eq. 5, the flux E_{ma} ($\mathrm{kg\ m^{-2}\ s^{-1}}$) depends on the fuel relative humidity (RH_m (%)), saturation specific humidity (q_{sat} (kg $\mathrm{kg^{-1}}$)), specific humidity of air (q (kg $\mathrm{kg^{-1}}$)), the surface conductance ($K_{ma,E}$ (m $\mathrm{s^{-1}}$)), and density of air (ρ_{air} (kg $\mathrm{m^{-3}}$)). RH_m is obtained by using the equilibrium fuel moisture content model of Nelson (1984) and is a function of FMC and temperature of the solid phase of the fuel (T_m (K)) (note: T_m is the temperature of the solid phase of the porous fuel in Matthews (2006) model and is different than T_s, which is the temperature of non-porous fuel used in baseline FDS (Eq. 1)). Similarly, in Eq. 6, the flux E_{la} (kg $\mathrm{m^{-2}s^{-1}}$) is proportional to the conductance ($K_{la,E}$ ($\mathrm{m\ s^{-1}}$)) and density of air and the difference between the saturation specific humidity of water (q_{sat}) and the specific humidity of air (q).

$$E_{ma} = \rho_{air} K_{ma,E} (RH_m \,.\, q_{sat} - q) \tag{5}$$

$$E_{la} = \rho_{air} K_{la,E} (q_{sat} - q) \tag{6}$$

Besides evaporation, the liquid water is absorbed by the solid fuel until the solid fuel reaches saturation. The moisture flux exchange between the solid fuel and liquid water (E_{ml} (kg $\mathrm{m^{-2}s^{-1}}$)) is determined by Eq. 7 from the density of solid fuel (ρ_s (kg $\mathrm{m^{-3}}$)), surface area to volume ratio of the fuel (μ ($\mathrm{m^{-1}}$)), fuel moisture content (fmc (kg $\mathrm{kg^{-1}}$)), and the empirical parameters L_a ($\mathrm{kg\ kg^{-1}}$) and L_b (kg $\mathrm{kg^{-1}}$). The empirical parameters L_a and L_b are obtained by fitting a correlation to the experimentally observed absorption curve of liquid water in fine litter fuel (Fig. 2 in Matthews, 2006).

$$E_{ml} = \frac{-\rho_s}{\mu} L_a exp\left(\frac{L_b - fmc}{L_a}\right) \tag{7}$$

Analogous to the moisture flux exchange is the heat flux exchange between the fuel components at each fuel layer. The sensible heat flux exchange at the interface of solid fuel with air and liquid water with air within the porous fuel are, respectively, given by the flux terms H_{ma} (W m^{-2}; Eq. 8) and H_{la} (W m^{-2}; Eq. 9). H_{ma} depends on the density and specific heat (C_p (J kg^{-1} K^{-1})) of air, conductance ($K_{ma,H}$) of heat flux from solid fuel to air, and the difference between the solid and air temperatures (T_m and T_a (K), respectively). Similarly, H_{la} is proportional to the density and specific heat of air, conductance of heat flux from liquid water to air ($K_{la,H}$), and the difference between the liquid water temperature (T_l (K)) and air temperature.

$$H_{ma} = \rho_{air}\, C_p\, K_{ma,H}\, (T_m - T_a) \tag{8}$$

$$H_{la} = \rho_{air}\, C_p\, K_{la,H}\, (T_l - T_a) \tag{9}$$

In the same way, the conductive heat flux between solid and liquid H_{ml} (W m^{-2}; Eq. 10), depends on the heat conductance from solid to liquid water ($K_{ml,H}$) and the difference in temperature of the solid and liquid water.

$$H_{ml} = K_{ml,H}(T_m - T_l) \tag{10}$$

Equations 5 – 7 describe the moisture flux exchange and Eq. 8 – 10 describe the heat flux exchange between solid, air, and liquid within each layer of the porous fuel. In addition to these fluxes, the heat and moisture exchanges also occur vertically between fuel layers. These exchanges include the net radiative heat transfer (R_{net} (W m^{-2})), the heat fluxes due to conduction in solid (H_C (W m^{-2})) and in the air spaces (H_T (W m^{-2})), the mass flux between air spaces (E_T (kg m^{-2} s^{-1})), and drainage of rainfall (D (kg m^{-2}s^{-1})). The vertical conductive heat and mass fluxes H_C, H_T, and E_T are, respectively, proportional to the vertical gradients of fuel temperature, air temperature, and specific humidity of air between the fuel layers. To estimate rainfall drainage, the model operates on the premise that each fuel layer intercepts a portion of rainfall proportional to its storage capacity (D_s (kg kg^{-1})), with any surplus water passing on to the layer beneath, based on the modified drainage flux (Rutters et al., 1971). More details of these terms can be found in Matthews (2006).

For each fuel layer, the model solves six interrelated equations: energy balance and moisture balance equations for the three components (solid, gas, and liquid) of the fuel layers. The energy balance equations for the fuel's solid (Eq. 11), air spaces (Eq. 12), and liquid water (Eq. 13), respectively, provide the solid fuel temperature (T_m), air temperature (T_a), and liquid water temperature (T_l) in each fuel layer.

$$C_{h,m}\frac{\partial T_m}{\partial t}=\frac{1}{V_m}\left(\frac{\partial R_{net}}{\partial z}+\frac{\partial H_C}{\partial z}\right)-\mu_{m,a}H_{ma}-\mu_{m,a}\lambda E_{ma}-\mu_{m,l}H_{ml} \tag{11}$$

$$\rho_{air}C_p\frac{\partial T_a}{\partial t}=\frac{1}{V_a}\frac{\partial H_T}{\partial z}+\mu_{a,m}H_{ma}+\mu_{a,l}H_{la} \tag{12}$$

$$C_{h,l}\frac{\partial T_l}{\partial t}=-\mu_{l,a}H_{la}-\mu_{l,a}\lambda E_{la}+\mu_{l,m}H_{ml} \tag{13}$$

The variation in temperature of the solid fuel (in Eq. 11) is governed by the net radiative heat fluxes (R_{net}), including both shortwave and longwave radiations, heat fluxes due to conduction (H_C), sensible heat flux exchanges between the solid fuel and air spaces (H_{ma}; Eq. 8) and between the solid fuel and liquid water (H_{ml}; Eq. 10), and the latent heat exchanges between the solid fuel and air spaces (λE_{ma}, with λ (J kg^{-1}) being the latent heat of water vaporization). The variation in the air temperature inside each porous fuel layer (in Eq. 12) is regulated by the conductive heat fluxes (H_T), sensible heat exchanges between the solid fuel and air spaces (H_{ma}) and between the free liquid water and air spaces (H_{la}; Eq. 9). The temperature of the liquid water inside the fuel layers (based on Eq. 13) varies due to the sensible heat exchanges between the liquid water and air spaces (H_{la}) and between the liquid water and solid fuel (H_{ml}), and the latent heat exchanges between the liquid water and the air spaces (λE_{la}). In the above equations, $C_{h,m}$ (J m^{-3}K^{-1}) and $C_{h,l}$ (J m^{-3}K^{-1}) are, respectively, the volumetric heat capacities of solid fuel and water. The terms V_m (m^3 m^{-3}) and V_a (m^3 m^{-3}) are the volumetric fraction of solid fuel and air, respectively, and $\mu_{x,y}$ (m^{-1}) represents the surface area-to-volume ratio of medium x for fluxes to/from medium y. As mentioned above, subscripts $m, a,$ and l represent the mediums of the porous fuel, i.e., solid fuel, air spaces, and liquid water, respectively. Lastly, z (m) corresponds to the depth of the fuel layer and t (s) is the time.

The moisture balance equations for the solid medium (Eq. 14), air spaces (Eq. 15), and liquid water (Eq. 16), respectively, provide the FMC (fmc), specific humidity of air spaces (q), and liquid water content (lw) in each fuel layer.

$$\rho_s \frac{\partial(fmc)}{\partial t} = -\mu_{m,a}E_{ma} - \mu_{m,l}E_{ml} \tag{14}$$

$$\rho_{air} \frac{\partial q}{\partial t} = \frac{1}{V_a}\frac{\partial E_T}{\partial z} + \mu_{a,m}E_{ma} + \mu_{a,l}E_{la} \tag{15}$$

$$\frac{\partial(lw)}{\partial t} = \frac{\partial D}{\partial z} + \mu_{l,m}E_{ml} - \mu_{l,a}E_{la} \tag{16}$$

The variation in FMC (Eq. 14) occurs due to the moisture flux exchanges between the solid fuel and air spaces (E_{ma}) and the absorption of liquid water in the solid fuel (E_{ml}). The specific humidity of air spaces (Eq. 15) changes due to the moisture exchanges between layers of the fuel (E_T), moisture flux exchanges between the solid fuel and air spaces (E_{ma}), and evaporation of liquid water (E_{la}). The amount of liquid water in the fuel layers (Eq. 16) varies due to the interception and drainage of rainfall (D), the liquid water absorbed in the solid fuel (E_{ml}), and the water evaporated into the air spaces (E_{la}).

The two sets of the energy and moisture equations (i.e., Eq. 11 – 16) are interrelated by exchanging the information of the water vapor flux from the solid fuel to the air spaces (E_{ma}) and the liquid water evaporated into the air spaces (E_{la}). In the above equations, ρ_s is the density of solid fuel. Once the amount of FMC (fmc) is calculated, the reaction rate for evaporation, $R'_{H_2O} = \rho_s(\partial(fmc)/\partial t)$ is found to replace the evaporation reaction rate found by the Arrhenius equation (Eq. 2) in FDS at each time step. The above set of interrelated equations is solved in FORTRAN, using backward finite differencing in space and advances in time using the Newton-Raphson method.

The two-way coupling of the thermodynamic-based FMC model and FDS fire-atmosphere interaction model

The FMC model requires specific boundary conditions to find the instantaneous fuel moisture at each fuel grid cell. These boundary conditions include radiation (R_{net}) at the fuel surface (for Eq. 11), fuel surface temperature (for Eq. 11), wind speed (for terms H_T, E_T, H_{ma} and H_{la} in Eq. 11-13 & 15), air temperature (for Eq. 12), relative humidity (for term E_T in Eq. 15), and precipitation (for term D in 16). For pre-fire conditions, the hourly local solar flux, wind speed, temperature, and relative humidity are obtained from meteorological data via weather data files by the National Renewable Energy Laboratory (NREL) (i.e., Himawari 2011-15: Physical Solar Model (PSM), version 3). While during fire the effects of these meteorological conditions can be impeded by fire-induced effects, they are significant for determining the fuel condition before fire, depending on the geographical location, and time of the day and year. During fire, the local and instantaneous net radiative heat fluxes, turbulent air temperature and wind speed, and relative humidity that are affected by the presence of fire are found at the first grid point in the gas phase above the solid fuel in FDS and fed into the FMC model at each time step. Besides boundary conditions, the FMC model sources the local and instantaneous values of solid fuel density (ρ_s; Eq. 4) from FDS. The spatiotemporally varying fuel-layers-average FMC found in the FMC model is then fed into FDS, where it updates the evaporation reaction rate (R_{H_2O}), the volumetric-averaged fuel density, specific heat, and thermal conductivity of the fuel, and the decomposition of fuel. Since FDS considers fuel as a pure solid substance without voids, the evaporation and condensation processes are treated as surface phenomena in it. Conversely, the thermodynamic-based FMC model treats fuel as a multi-layer porous medium, each composed of solid, liquid, and air spaces, where the evaporation and condensation processes occur inside the fuel layers. For the coupling process, therefore, a fuel-layer-average moisture value calculated as $\frac{1}{N}\sum_1^N(fmc)$, with N being the number of fuel layers, was used to calculate R'_{H_2O} to be supplied to FDS in Eq. 1, where the fuel sees the effect of fire to find the fuel temperature (T_s).

Model Validation

In this section, validation studies of the thermodynamic-based FMC prediction model, and the coupled FDS + FMC model are provided. Even though the baseline FDS model is validated for its different aspects in previous literature, we performed additional validation studies to test its accuracy under daytime atmospheric conditions and on capturing flow physics over non-flat surface topographies in the absence of fire. These validation studies are provided in Appendix A.

Validation of the FMC model

In this validation study, the measured data reported by McCaw (1997) was used. The observed data was recorded in April 1996 near Perup in southwest Western Australia over dead fuel of $0.01 - 0.03$ m thickness. The fuel consisted of Eucalyptus leaves and shrubs, with an average thickness of 0.02 m. The tree canopy at the location was 4 m high with 40% canopy closure. The air temperature and relative humidity data for three consecutive days that were recorded at 2 m height (Matthews, 2006) was used as inputs in the model. The model also requires wind speed and solar radiation data as inputs. However, these required data were not provided in the literature. Therefore, they were obtained from the first accessible data from Himawari 2011-15: PSM v3 weather data file for the year 2011. For the same month of April in 2011, the days with temperature and relative humidity close to the recorded temperature and humidity data reported in Matthews (2006) were identified and the hourly mean diurnal solar radiation and wind speed of those days were calculated. Following Matthews (2006), the soil temperature was assumed to be equal to the air temperature and there was no moisture flux exchange between the soil and fuel. The vegetation characteristics were obtained from Matthews (2006) and are provided in Appendix B.

Figure 1 shows a comparison of the model prediction for FMC against measured data by McCaw (1997) and model prediction by Matthews (2006). To quantify the prediction accuracy, the root mean square error (RMSE) of the predicted values was also estimated, indicating a small error of 0.024 kg kg^{-1}. We suspect that the potential source of the slight differences seen here is the input parameters of solar radiation and wind speed, which were approximated from the weather data file of a different year, due to unavailability.

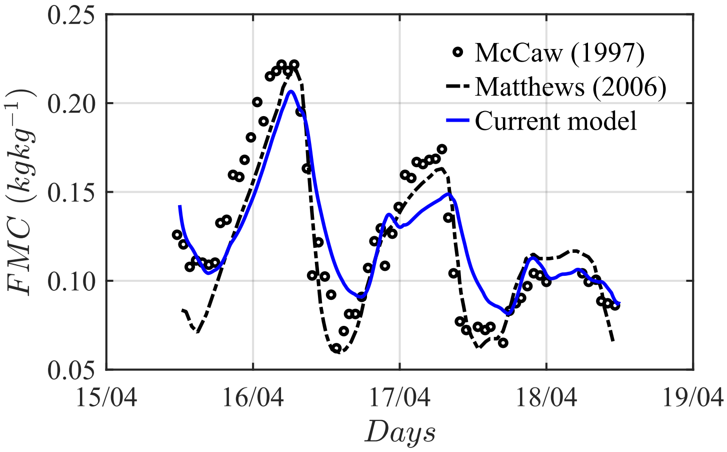

Fig. 1: Comparison of predicted and experimentally observed temporal variation of surface fuel moisture content (FMC) for three consecutive days in Perup Western Australia.

Validation of the new model

In this section, we conduct three validation studies to investigate the accuracy of the new two-way coupled FDS + FMC model in predicting the rate of flame spread and heat release rate (HRR).

In these studies, we used the experimental data of Korobeinichev et al. (2022), Perez-Ramirez et al. (2017), and Catchpole et al. (1998). It should be noted that, in general, there is a dearth in the existence of experimental data with proper details on the effect of fuel moisture on fire propagation that could be used for the validation study in this work.

Validation study 1: Testing the flame spread rate in a small pine needle fuel bed

In this study, the new model is validated against the flame propagation experiment of Korobeinichev et al. (2022) that was performed on a pine needle fuel bed of 0.02 m height in a chamber of dimension 0.7 m (streamwise) × 0.34 m (spanwise) × 0.3 m (vertical). The fuel bed was laid over an asbestos substrate, which was placed on the lower surface of the chamber. The experiments were conducted using fuel beds of varying widths, namely 0.08 m and 0.2 m, with a fixed bed length of 0.5 m. Fire clay walls, each 0.02 m in height, were erected on both sides of the fuel bed to contain the combustion process. The fuel bed was located 0.1 m from the inlet and outlet of the chamber (Fig. 2 of Korobeinichev et al. (2022)). The air flow inside the chamber was generated by a fan with a maximum flow rate of 0.11 m^3 s^{-1}. The air was passed through an expanding circular channel and through a porous channel to ensure the flow was laminar as it entered the chamber. The position of the flame front, required to determine the rate of flame spread, was recorded using two cameras positioned to capture both frontal and overhead perspectives.

As stated by Korobeinichev et al. (2022), in the 0.08 m wide fuel bed, the flame intensity was less, which led to reduced preheating of fuel as compared to the 0.2 m wide fuel bed. Consequently, for the 0.08 m wide bed, the flame rate of spread was more sensitive to fuel moisture (that remained in the fuel after preheating) in contrast to the 0.2 m wide bed. In addition, it is reported that, for the 0.08 m width fuel bed at a wind speed of 0.4 m s^{-1}, the baseline FDS model underpredicts the rate of spread (Korobeinichev et al., 2022), thus, this case was chosen to investigate whether the new model can improve the baseline FDS prediction.

The pine needles in the computational domain were represented as a collection of fixed cylindrical lagrangian particles. As the flame approaches the needles, it decomposes the fuel into water vapor, pyrolysis gases, char, and residue following infinite-rate chemistry. The properties of the fuel, char, and pyrolysis gases were obtained from Korobeinichev et al. (2022) and are provided in Appendix C. The ambient air at 300 K entered the domain from the left boundary at a uniform velocity of 0.4 m s^{-1}. The right boundary was at outflow condition with constant pressure. All other boundaries of the chamber were considered as no-slip walls with a constant temperature of 294.15 K. As in Korobeinichev et al. (2022), the fuel bed was ignited using a constant temperature heating plate maintained at 1573.15 K for 2.5 s at a distance of 0.002 m upstream of the leading edge of the fuel bed. A sensitivity analysis indicated that a grid resolution of 0.005 m (streamwise), 0.01 m (spanwise), and 0.006 m (vertical) was fine enough for this simulation.

Following Korobeinichev et al. (2022), the rate of flame spread was determined by the average of the time taken for the flame front to travel each 0.1 m section of the fuel bed after it reached 0.2 m from the leading edge. As reported by Korobeinichev et al. (2022), the flame rate of spread in the wind-tunnel experiment was 6 mm s^{-1}, while the rate of spread predicted by the baseline FDS was 4 mm s^{-1}. Our simulation, using the new model improved the baseline FDS prediction by 20%, yielding a spread rate of 4.8 mm s^{-1}. While with the new model the prediction of the flame spread rate improves, we believe that the general underprediction of both the baseline and modified FDS models involves factors other than fuel moisture.

Validation study 2: Heat release rate in a pine needle fuel bed measured in a furniture calorimeter

A second study was conducted to investigate the accuracy of the new model against the experiments of Perez-Ramirez et al. (2017). The experiments were performed for a 2 m long and 1 m wide pine needle fuel bed located inside a 1 MW furniture calorimeter with three combinations of fuel loading and fuel height (Table 1 of Perez-Ramirez et al., 2017). The fuel bed was situated within a 3 m × 3 m hood with 1 m^3 s^{-1} extraction system. A line fire was ignited along the width of the fuel bed to observe the flame spread rate. Combustion gases (carbon monoxide and carbon dioxide) and oxygen in the exhaust pipe were analyzed during each experiment to calculate the heat release and mass loss rates using the oxygen consumption calorimetry technique.

In Perez-Ramirez et al. (2017), the HRR (kW) for all experiment scenarios was compared against the numerically predicted HRR by the Wildland-urban interface Fire Dynamics Simulator (WFDS) model (a previous version of the FDS model). WFDS, like FDS, uses the Arrhenius approach to model the fuel drying process. For two of these cases, the mass loss rate (MLR; kg s^{-1}) for one (out of four) experiment was underpredicted by WFDS at the beginning of pyrolysis and during the extinction phase. The study reports that the underprediction of MLR by WFDS during the extinction phase was because the single-step reaction was unable to capture the char oxidation while it does not discuss the reason for the initial underprediction of MLR. We hypothesize that the underestimation of the MLR by WFDS at the beginning of pyrolysis is related to the Arrhenius fuel drying model. To investigate whether the new model can improve the baseline Arrhenius prediction of MLR and HRR, two cases with 1) fuel loading of 1.2 kg m^{-2} and fuel bed height of 0.065 m and 2) fuel loading of 0.9 kg m^{-2} and fuel height of 0.055 m were studied. For the sake of brevity and due to the similarity of the trends, only the results of the first case are shown here.

In line with Perez-Ramirez et al. (2017), the pine needle fuel bed in the simulation was located under a 3 m × 3 m hood in a domain of 3 m (streamwise) × 3 m (spanwise) × 3.84 m (vertical), representing the furniture calorimeter. The fuel bed in the domain was represented as a collection of fixed cylindrical lagrangian particles. Details of the fuel bed configuration and thermo-physical properties of the solid and gas phases were obtained from Perez-Ramirez et al. (2017) and are provided in Appendix D. The streamwise and spanwise boundaries were at inflow-outflow conditions. The hood was represented by multiple stepwise obstacles with a constant volume flow rate of 1 m^3 s^{-1}. As in Perez-Ramirez et al. (2017), the fuel bed was ignited by ignitor particles arranged in a 0.004 m × 1 m area located upstream of the fuel bed and maintained at 1273.15 K. A uniform grid size of 0.02 m in all directions was used based on the result of the grid independency study conducted by Perez-Ramirez et al. (2017). The 0.02 m grid size is reported to be sufficient to model the flow velocity in the hood (Perez-Ramirez et al., 2014). This grid size is also less than the extinction length (Morvan, 2011) derived based on the volume fraction and surface area-to-volume ratio of the fuel.

The total HRR (kW), which is the combination of heat released from the flaming and smoldering combustion, was predicted, and compared against the experimental results in Fig. 2a. It was observed that as the fire approached a quasi-steady rate of spread (characterized by nearly constant total HRR), 60 – 75% of the total HRR stemmed from the flaming combustion phase. The HRR obtained using the new model shows higher magnitudes compared to those obtained from the baseline FDS model using the Arrhenius approach and is in closer agreement with the experimentally measured HRR values. This is because, in the new model, unlike the baseline model, localized regions of low fuel moisture in front of the fire were significantly more pronounced due to the more effective preheating of the fuel. As a consequence, when fire reaches the fuel, less thermal energy is used for drying the solid fuel particles in the new model resulting in an increase in the fire intensity and HRR. In the same way, the prediction of MLR (kg s^{-1}) using the new model improved, showing closer agreements with the experimental results (Fig. 2b). In general, HRR and MLR exhibit significant variations throughout the fire progression. These quantities increase, reach a quasi-steady state, and then decline to zero. To assess this variability, a moving standard deviation was also calculated using a sliding window of 5 seconds. The moving standard deviation for the HRR for both the baseline and new models ranged from 1.58 to 1.585 kW, while for the mass loss rate, it varied between 0.0001 and 0.0048 kg s^{-1}. Similar improved trends in the prediction of HRR and MLR were observed for the case with a fuel loading of 0.9 kg m^{-2} and fuel height of 0.055 m (not shown).

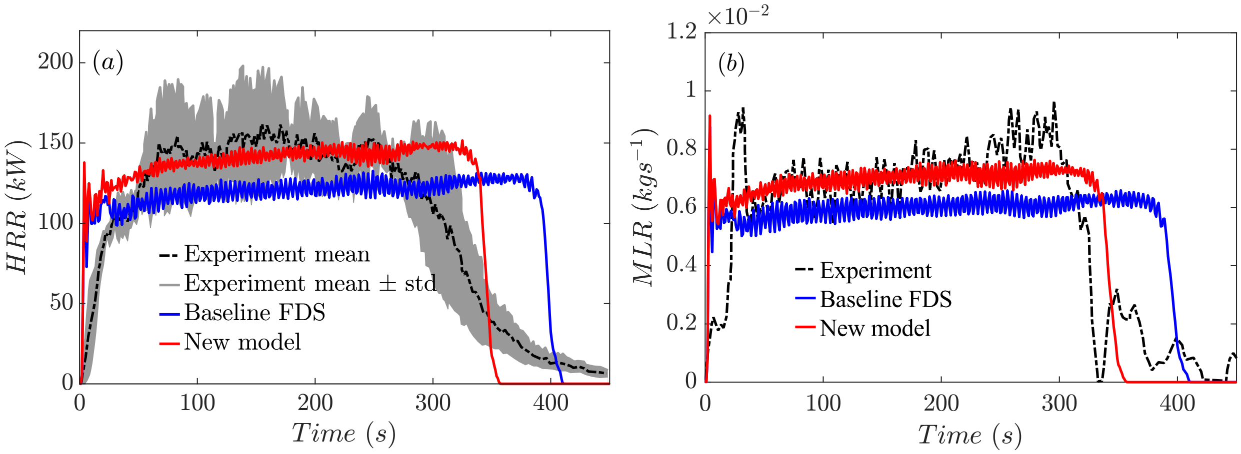

Fig. 2: Temporal variation of the modeled and experimental (a) heat release rate (HRR) and (b) mass loss rate (MLR).

Validation study 3: Testing fire propagation in an excelsior fuel bed

This study evaluated the accuracy of the new model by comparing it to the experiments conducted by Catchpole et al. (1998), specifically in assessing the fire rate of spread across a range of FMC conditions. Catchpole et al. (1998) conducted 357 experiments in a wind tunnel of dimensions 12 m (length) × 3 m (width) × 3 m (height) to obtain the rate of spread for several combinations of fuel moisture, wind speeds, and fuel properties (depth, particle sizes, and packing ratio). The length of the fuel bed varied between 5 m and 8 m in different experiments. Metal strips, matching the fuel bed length, were placed along the sides of the fuel bed to prevent air from entering the combustion zone. At the tunnel inlet, wire mesh was placed to promote the development of turbulent boundary layer in the flow. The wind velocity inside the tunnel ranged between 0.0 and 3.1 m s^{-1} in the free stream above the boundary layer for different sets of experiments. The fuel was pre-conditioned to achieve the specified moisture content for each experiment. Among all experimental scenarios, in four cases, wind speed and all fuel properties were held constant, while the FMC varied between 18.1% (EXMC48), 10.1% (EXMC36), 5.5% (EXMC23), and 3% (EXMC69). Within this group, case EXMC36, with a FMC of 10.1% indicated a lower rate of fire spread compared to that of case EXMC48 with a higher FMC of 18.1%. Therefore, case EXMC36 was considered as an outlier and not used in the comparison study.

In accordance with Catchpole et al. (1998), a simulation was conducted featuring an 8 m long and 1 m wide fuel bed with a height of 0.203 m, composed of regular excelsior. The fuel was represented as a collection of fixed Lagrangian particles with a packing ratio of 0.005. Positioned 2 m from the domain inlet, the fuel bed was equipped with a baffle upstream and walls on both sides with heights matching the height of the fuel bed. In the streamwise direction, inflow-outflow boundary conditions were specified, incorporating an inlet wind velocity of 2.68 m s^{-1}. The configuration details of the fuel bed, along with the thermo-physical properties of the solid and gas phases, were sourced from the FDS version v6.8.0 validation repository, as provided in Appendix E. The fuel bed was ignited by a plate measuring 0.05 m in length and 1 m in width, subjected to a heating rate of 800 kW m^{-2} for a duration of 10 seconds. A uniform grid size of 0.05 m was employed in all directions, adhering to the maximum grid size constraints based on the extinction length criteria (0.1 m).

Consistent with the experiments, the rate of spread was determined by evaluating the average of the time taken for the fire to travel each 0.5 m section of the fuel bed after it reached a quasi-steady rate of spread at 4.5 m from the leading edge. The comparison of the modeled and observed average rate of spread for the three cases is shown in Table 1. The results indicate that the new model improved the baseline FDS prediction, respectively, by 14.21%, 7.9%, and 1.16% for EXMC69, EXMC23, and EXMC48 cases. The results of both the baseline and new models showed similar standard deviations in the range of 0.027 – 0.043.

Table 1: Comparison of the modeled (using the baseline FDS and the new FDS + FMC models) and observed (Catchpole et al., 1998) average rate of spreads for fuels with different FMCs.

Cases	FMC (%)	Rate of spread (m s^{-1})		
		Experiment	Baseline FDS	New model
EXMC69	3.0	0.242	0.211	0.241
EXMC23	5.5	0.252	0.202	0.218

EXMC48	18.1	0.175	0.171	0.173

A Case Study: FMC Response to Instantaneous Turbulence and its Effect on Fire and Plume Behavior

While this work focuses on the description of a new physics-based fuel moisture model coupled with the FDS fire-atmosphere interaction model, an application of the model is briefly described here. The experimental setup of Korobeinichev et al. (2022) (described in Validation Study 1) was used as a case study and the results pertinent to the spatiotemporal variation of FMC and fire and plume behaviors are briefly discussed below.

Spatiotemporal Variations of FMC

To investigate the spatiotemporal variations of FMC, virtual probes were introduced on the fuel bed at five locations in the streamwise direction at the mid-span of the domain (i.e., $y/h = 0$, with h being the fuel height). Figure 3 compares the FMC variations with time from the baseline FDS model (Fig. 3a) with those of the new model (Fig. 3b). Comparison of the figures shows that the drop in FMC from its initial value starts with delays in the new model compared to the baseline FDS model. Following that, the two models continue showing different drying behaviors with time. The baseline model indicates quick plunges in the moisture levels at all locations that takes approximately 18 s from the beginning of drying to the complete evaporation of the fuel moisture. However, in the new model, the drying process indicates a gradual and different behavior: At $x/h = 10$, and 15, complete drying happened in 25 s, indicating an increase of 38% in drying time compared to that of the baseline model at the same locations. At $x/h = 20, 25$, and 30, we noticed a small rise of 1.5% in FMC from the baseline value of 0.065 kg kg^{-1} before the flame reaches the (virtual) probes at these locations. This rise in the local FMC is due to the addition of water vapor to the gas phase during combustion, which causes an increase in the relative humidity of the ambient air. Because of this, a positive water vapor flux exchange occurred from the ambient air to the fuel, raising the FMC at these locations. The amount of this moisture rise in fuel, in general, depends on several environmental factors that control the concentration of water vapor over the fuel layer. The observed increase in fuel moisture is consistent with the observations by Zhao et al. (2021), who investigated the dynamic variations of FMC in wood pellets in a domestic stove. The rise in FMC at $x/h = 20, 25$, and 30 led to an increase in the fuel drying time to approximately 30 s. It should be noted that the increase in local relative humidity and its effect on FMC is not captured by the Arrhenius drying model in the baseline model. Our investigation confirms that the delay in the drop of FMC from its initial value in the new model is also due to this process.

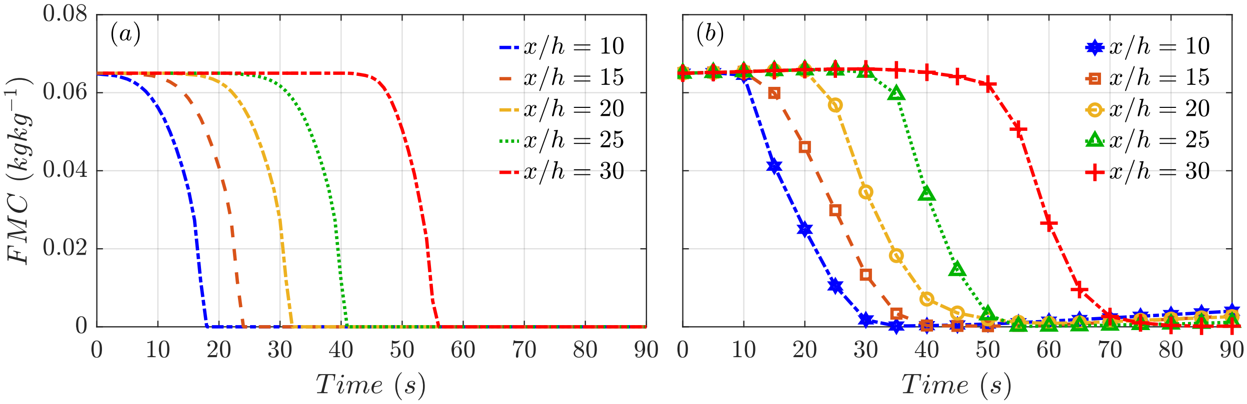

Fig. 3: Temporal variations of FMC in the fuel bed (following the setup of Korobeinichev et al., 2022) at $x/h = 10, 15, 20, 25$, and 30 along $y/h = 0$, simulated by (a) the baseline FDS model and (b) the new model.

Fire and plume behaviors

Figure 4 compares the temporal evolution of the fuel surface temperature at two locations in the streamwise direction (i.e., $x/h = 20$ and 25) at the mid-span of the domain. The two peaks in temperature in Fig. 4a correspond to the time when the leading and the trailing edges of the flame pass location $x/h = 20$. It can be noticed that, in the new model, the fuel temperature at both locations rises above that of the baseline FDS after around 40 s into the fire propagation and after the flame had enough time to thermally interact with the fuel ahead of the fire front. We speculate that the occurrence of higher fuel temperature in the new model is due to the lower evaporation rate in this case (Fig. 3), indicating lesser energy going to evaporating water and thus more energy spent on increasing the whole fuel temperature, which also influences the reaction rate of pyrolysis.

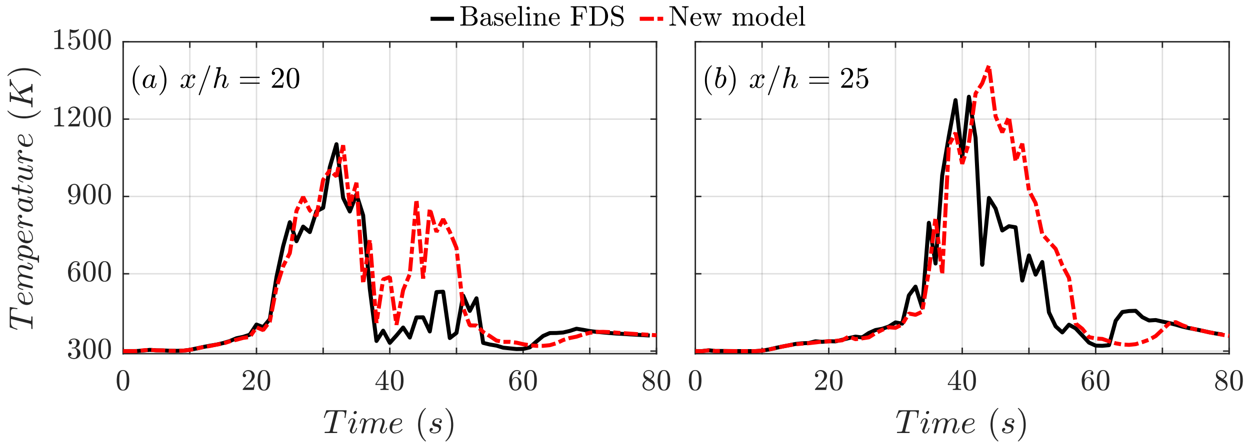

Fig. 4: Temporal variations of fuel surface temperature at $x/h = 20$, and 25 along $y/h = 0$.

To investigate how the thermodynamic variations of FMC influences the plume behavior, the Byram convection number, which indicates the ratio of the power of fire to the power of the wind was investigated for the two cases using Eq. 17 (Finney et al., 2021; Korobeinichev et al., 2022).

$$N_s = \frac{2gI}{\rho_\infty (U_\infty - ROS)^3 C_p T_\infty} \tag{17}$$

In this equation, ρ_∞ (kg m^{-3}), U_∞ (m s^{-1}), C_p (J kg^{-1}K^{-1}), and T_∞ (K) are the density, velocity magnitude, specific heat, and temperature of the air, respectively. g (m s^{-2}) is the acceleration due to gravity, I (W m^{-1}) is the intensity of the fire line, and ROS (m s^{-1}) is the fire rate of spread. The Byram number was calculated at the same locations where the rate of spread was found (i.e., $x/h =$ 20, 25, 30), and the average of these values was then used for comparison between the two cases. The Byram number for the baseline FDS case is 8.24, while it rises to 10.97 for the new model, indicating a higher power of buoyancy force as compared to the power of inertial force, and thus a more plume-dominated rather than a wind-driven fire in the new model. This is also evident when comparing the trajectory of the flame and plume throughout the course of the fire propagation and the average plume angle between the two cases. To calculate the average plume angle, the iso-contour of carbon dioxide mass fraction at 0.05 kg kg^{-1} was examined for the time when the fire passed across the length of the fuel bed from $x/h = 5$ to $x/h =$ 30. The average plume angle was then determined from the angle formed by the line connecting the plume base center (i.e., the center of the flame depth) to the rightmost top edge of the plume with respect to the fuel surface. Notably, in the baseline FDS, the average plume angle was observed to be 6.63°

less than the corresponding angle of 27.29° in the new model. The magnitude of the average plume angle changes for both cases when different carbon dioxide mass fraction values are used to define the plume's boundary. Nevertheless, across all scenarios, the average angle that the plume formed with the surface in the new model consistently exceeded that of the baseline FDS.

Summary

This paper introduces a comprehensive physics-based model that integrates a thermodynamic-driven prediction model for dead fuel moisture content (FMC) with the Fire Dynamics Simulator (FDS) of the National Institute of Standards and Technology. The motivation for developing this model arises from the existing modeling limitations, where fuel drying is often treated as a kinetic process, whereas in nature, it is a thermodynamic process. Unlike the kinetic process, in the thermodynamic process, the phase change nature of moisture evaporation and the coexistence of liquid water and water vapor in the porous layers of the fuel, together with the complex interchanging processes of mass and heat transport between the porous fuel layers are considered. Such a capability is important in fire-safety research, especially where small-scale variations in fire dynamics are important.

Following tests of the sub-models, the accuracy of the whole new FMC + FDS model for predicting HRR and MLR was tested against the experimental data by Korobeinichev et al. (2022), Perez-Ramirez et al. (2017), and Catchpole et al. (1998). The validation results indicated improvements over the baseline model. Given the absence of additional measured data providing essential details, the model tests were constrained to the scenarios mentioned above. However, more tests are desired to identify potential model weaknesses and to explore the breadth of model performance across various environmental, material, and geometrical conditions.

The paper also includes a case study on flame propagation in a small fuel bed, showcasing the enhanced efficacy of the new model and its unique ability to depict intricate processes such as moisture exchanges with the ambient atmosphere (a process that cannot be captured by a kinetic-based model). The results of our case study also indicated that the kinetic-based FMC model (in the baseline FDS model) and thermodynamic-based FMC model (in the new FMC + FDS model) result in different fuel drying behavior, fire spread, fuel temperature, and plume dynamics. Further studies, however, are required in different scales to better understand the differences between the models and the extent of the effect of FMC model choice. The model can be improved in several aspects; however, the large number of input parameters and the computational costs of the simulations are the main limiting factors (which are shared between all physics-based models). For large domains, under realistic atmospheric conditions with enough grid resolutions, the computational costs can be significant, limiting the application of the model.

Acknowledgment

This work is supported by funding from the Department of Defense Strategic Environmental Research and Development Program (SERDP) grant number RC20-1298 and National Science Foundation (NSF) grant number CBET 2043103. In addition, this research used resources of the National Energy Research Scientific Computing Center, a DOE Office of Science User Facility supported by the Office of Science of the U.S. Department of Energy under Contract No. DE-AC02-05CH11231 using NERSC award BER-ERCAP0022408. We would also like to acknowledge high-performance computing support from Cheyenne (doi:10.5065/D6RX99HX) provided by NCAR's Computational and Information Systems Laboratory, sponsored by the National Science Foundation. We also thank Dr. William (Ruddy) Mell and Dr. Eric Mueller for their valuable input and for providing relevant references.

Appendix A: FDS model validation

A review of the literature indicates that there are several validation studies of FDS that test the model accuracy for predicting the heat release and mass loss rates of fuels (Meerpoel-Pietri et al., 2022; Perez-Ramirez et al., 2017), and the rate of fire spread (Mell et al., 2013). In this section, however, we conduct three studies to investigate the accuracy of the LES of FDS in predicting flow characteristics within channel flows affected by surface topographies (using laboratory data of Martinuzzi & Tropea (1993) and Meinders (1998)) and in convective atmospheric boundary layer flows (using field data of Lenschow et al. (1980)) in the absence of fire.

Channel flow with a surface-mounted obstacle

In this study, the experimental data obtained by Martinuzzi and Tropea (1993) and documented and used by Rodi et al. (1997) and Letzel et al. (2008) was utilized. The experimental setup included a surface-mounted obstacle of height H that was placed at a distance of $3H$ from the inflow boundary of a channel of height $2H$. Following the numerical study of Letzel et al. (2008), the domain length and width were taken to be $19H$ and $7H$, respectively, in the streamwise and spanwise directions. A uniform inflow velocity with a Reynolds number of 10^6 (based on H) was prescribed at the inlet and periodic boundary conditions were used in the streamwise and spanwise directions. The domain length was found to be long enough to eliminate the effects of the residual wake flow from the obstacle at the inlet due to the periodic boundary conditions. Through a sensitivity analysis, it was found that a grid size of $0.025H$ is adequate for these simulations.

The simulation was run for 5 hours to stabilize, and the results were time-averaged over the last 2 hours, equivalent to over 100 eddy turnover times in the domain. The time-averaged vertical profiles of streamwise velocities normalized by the bulk velocity at different locations in the streamwise direction were compared against the experimental data as shown in Fig. 5. The results indicate that FDS satisfactorily captures the flow features at different locations of the domain.

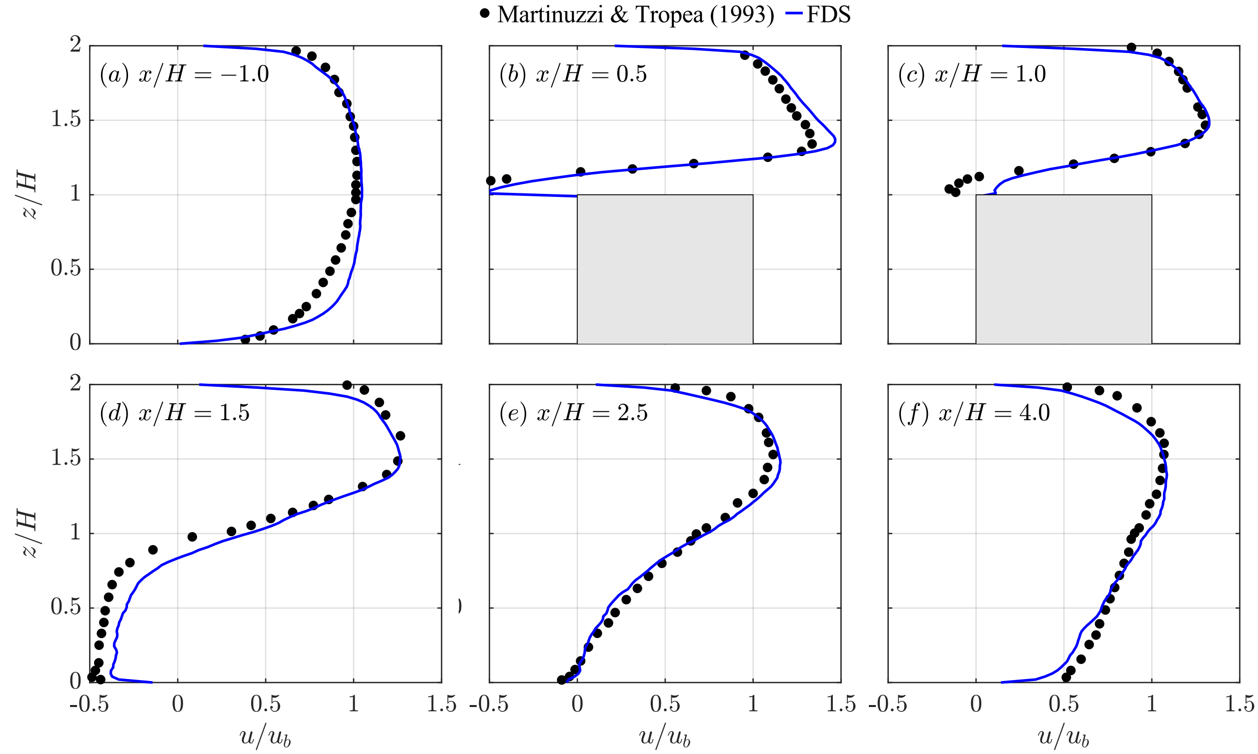

Fig. 5: Time-averaged vertical profiles of the normalized streamwise velocities at $y\ /\ H = 0$ and $x\ /\ H =$ -1, 0.5, 1, 1.5, 2.5, and 4. u_b is the bulk velocity.

Flow over an array of surface-mounted obstacles

In this validation study, flow measurements of Meinders (1998) were utilized. The experimental setup involved an array of 25 by 10 cubical obstacles of width H that were placed uniformly with a distance of $3H$ from each other in each horizontal direction. The obstacles were mounted at the bottom of a channel with a height of $3.4H$. The measurements were made in locations where a fully developed periodic flow was achieved. Following Tseng et al. (2006), a computational domain with a dimension of $12H$ (streamwise) × $12H$ (spanwise) × $3.4H$ (vertical) and consisting of a matrix of 3 by 3 cubes was chosen. Periodic and no-slip boundary conditions were, respectively, imposed in the horizontal directions and at the top and bottom boundaries. Through grid sensitivity analyses, a grid size of $0.05H$ was found to be fine enough for this simulation. A uniform inflow velocity was prescribed at the inlet according to the Reynolds number of 10^6 based on the obstacle height. The results were averaged over the last 4 hours (equivalent to over 100 eddy turnover times in the domain) of a 10-hour simulation, and mean streamwise and spanwise velocity profiles from various locations were compared against the experimental results. Figures 6a and 6b, respectively, compare the vertical and spanwise profiles of the mean streamwise velocities obtained from the $y/H = 0$ and $z/H = 0.5$ planes for the central cube at five different locations along the flow (i.e., $x/H = -0.3, 0.3, 1.3, 1.7,$ and 2.3). Figure 6c compares the mean spanwise velocities obtained at $z/H = 0.5$ for the central cube at five locations along the flow. The velocities are normalized by a reference velocity value obtained at (x/H, y/H, z/H) = (1.3, 0, 2.25). The FDS predicted mean streamwise and spanwise velocities agree well with the experimental data.

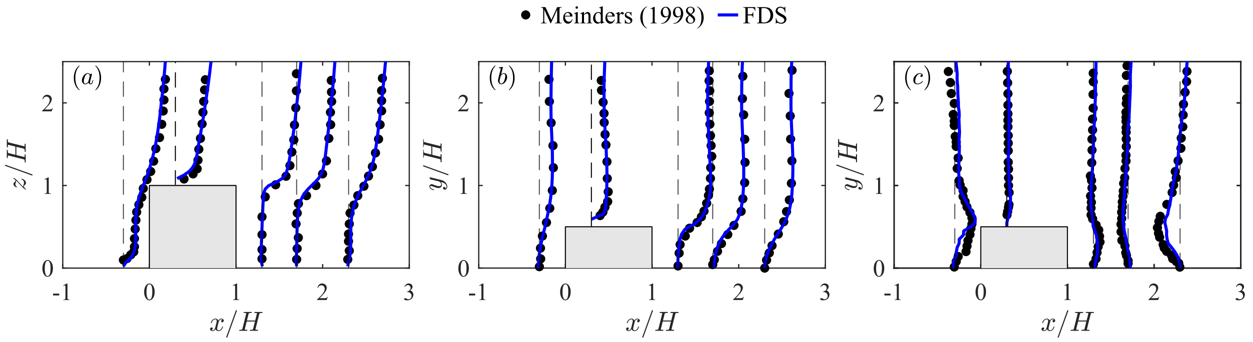

Fig 6: Time-averaged (a) streamwise velocity profiles from the vertical center plane at $y/H = 0$, (b) streamwise velocity profiles from the horizontal plane at half the obstacle height ($z/H = 0.5$), and (c) spanwise velocity profiles from the horizontal plane at $z/H = 0.5$.

Convective atmospheric boundary layer flow

Validation studies presented above are related to cases with neutrally stratified flows. To investigate the accuracy of FDS in predicting flow features under non-neutral stratified atmospheric boundary layer flows, field-measured data from Lenschow et al. (1980) and laboratory-measured data from Willis and Deardorff (1974) were used. Additionally, a comparison of the results was made against the numerical results of Raasch and Etling (1991). The computational domain was chosen to be a cuboid of dimension 3.2 km × 3.2 km × 4.8 km with a constant heat flux of 125 W m^{-2} imposed at the bottom boundary. The simulation was initialized by a flow at rest with an initial neutral temperature stratification till 800 m from the ground and a stable layer of 1 K ⁄100 m aloft. The results were averaged over the last 2 hours of a 6-hour simulation. Figure 7a compares the time and horizontally averaged profile of vertical heat flux normalized by the surface heat flux and Figs. 7b and 7c compare the time and horizontally averaged profiles of streamwise and vertical velocity variances normalized by the square of the convective velocity (w_*) against the experimental and numerical data. Overall, FDS captures the flow statistics satisfactorily. The slight differences in the results by FDS from the measured data are expected to be due to the energy equation that is not explicitly solved in the model.

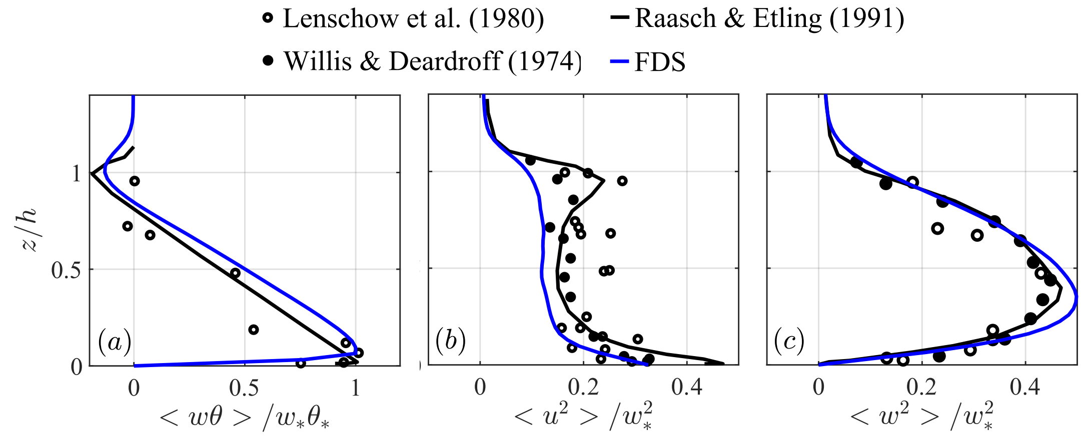

Fig. 7: Time and horizontally averaged profiles of normalized (a) vertical heat flux, (b) streamwise velocity variance, and (c) vertical velocity variance. w_* and θ_* are the characteristic velocity and potential temperature, respectively.

Appendix B: Parameters used in validation of the FMC model

Table 2: Parameters used to perform the validation of the moisture model (based on Table 1, and Appendix 1 of Matthews, 2006)

	Parameter	Unit	Value
Solid fuel	Height	m	0.02
	Bulk density	$\mathrm{kg\ m^{-3}}$	62
	Density (ρ_s)	$\mathrm{kg\ m^{-3}}$	550
	Surface area-to-volume ratio	$\mathrm{m^{-1}}$	3000
	Characteristic length	m	0.03
Solid fuel moisture	Nelson model parameter A	-	5.2
	Nelson model parameter B	-	-19
	Surface conductance ($K_{ma,E}$)	$\mathrm{m\ s^{-1}}$	0.0006
	Saturation moisture content	$\mathrm{kg\ kg^{-1}}$	1.4
	Liquid water absorption parameter L_a	$\mathrm{kg\ kg^{-1}}$	0.23
	Liquid water absorption parameter L_b	$\mathrm{kg\ kg^{-1}}$	-1.63
Radiation	Albedo	-	0.27
	Attenuation coefficient	-	1.363
Conduction	Heat conductivity as a function of moisture content k_{slope}	$\mathrm{Wm^{-1}K^{-1}}$	0.2
	Heat conductivity as a function of moisture content $k_{intercept}$	$\mathrm{Wm^{-1}K^{-1}}$	0.14
	Solid-to-water heat conductivity ($K_{ml,H}$)	$\mathrm{Wm^{-2}K^{-1}}$	700
Drainage	Rainfall storage capacity	$\mathrm{kg\ kg^{-1}}$	1.153
	Drainage coefficient	$\mathrm{s^{-1}}$	0.00003
Vertical mixing	Diffusivity at the top of the litter layer $D_{T0,a}$	$\mathrm{m^2s^{-1}}$	0.00002
	Diffusivity at the top of the litter layer $D_{T0,b}$	$\mathrm{s\ m^{-1}}$	2.60
	Diffusivity attenuation coefficient χ_a	-	2.08
	Diffusivity attenuation coefficient χ_b	$\mathrm{s\ m^{-1}}$	2.38
Soil	Albedo	-	0.2
	Field capacity	$\mathrm{m^2m^{-3}}$	0.3
Top boundary	Aerodynamic roughness length	m	0.01
	Screen height	m	2.0
Constants	Thermal diffusivity of air	$\mathrm{m^2s^{-1}}$	2.08×10^{-5}
	Diffusion coefficient of water vapor in the air	$\mathrm{m^2s^{-1}}$	2.34×10^{-5}
	Latent heat of vaporization of water (λ)	$\mathrm{J\ kg^{-1}}$	2.45×10^{6}
	Stefan-Boltzmann constant	$\mathrm{J\ m^{-2}K^{-4}}$	5.67×10^{-8}
	Volumetric heat capacity of water ($C_{h,l}$)	$\mathrm{J\ m^{-3}K^{-1}}$	4.3×10^{-6}
	Volumetric heat capacity of solid fuel ($C_{h,m}$)	$\mathrm{J\ m^{-3}K^{-1}}$	1.0×10^{6}
	Specific heat of air (C_p)	$\mathrm{J\ kg^{-1}K^{-1}}$	1004.5
	Von Karman constant		0.4
	Universal gas constant	$\mathrm{J\ mol^{-1}K^{-1}}$	8.314
	Molecular mass of water	$\mathrm{g\ mol^{-1}}$	18.0153

Appendix C Parameters used to validate the fully coupled model in Validation Study 1

Table 3: Parameters used to perform the validation of the fully coupled model (based on Table 1 of Korobeinichev et al., 2022)

	Parameter	Unit	Value
Solid fuel	Height	m	0.02
	Dry fuel density	kg m^{-3}	593
	Surface area-to-volume ratio	m^{-1}	4550
	Packing ratio	-	0.058
	Pre-exponential factor (A_{pyr})	s^{-1}	36,400
	Activation energy (E_{pyr})	Jmol^{-1}	60,276
	Heat of pyrolysis (ΔH_{pyr})	kJ kg^{-1}	418
	Mass fraction of dry fuel converted to char	-	0.18
Moisture	Fuel moisture content (for constant FMC case only)	m^{-1}	0.065
	Heat of vaporization of water(ΔH_{vap})	kJ kg^{-1}	2259
Char	Density	kg m^{-3}	300
	Thermal conductivity	Wm^{-1}K^{-1}	0.05
	Specific heat (As a function of temperature T)	kJ kg^{-1}K^{-1}	$0.42 + 0.002\ T + (6.85 \times 10^{-7})\ T^{2}$
	Pre-exponential factor (A_{char})	m s^{-1}	430
	Activation energy (E_{char})	Jmol^{-1}	-12,000
	Heat of formation (ΔH_{char})	kJ kg^{-1}	
	Mass fraction of char converted to ash	-	0.2
	Mass fraction of oxygen	-	1.65
Ash	Density	kg m^{-3}	67
	Thermal conductivity	Wm^{-1}K^{-1}	0.1
	Specific heat (As a function of temperature T)	kJ kg^{-1}K^{-1}	$1.244(T/300)^{0.315}$
Soot	Density	kg m^{-3}	1800
	Thermal conductivity	Wm^{-1}K^{-1}	0.55
	Specific heat	kJ kg^{-1}K^{-1}	2.1

Appendix D Parameters used to validate the fully coupled model in Validation Study 2

Table 4: Parameters used to perform the validation of the fully coupled model (based on Perez-Remirez et al., 2017)

	Parameter	Unit	Value
Solid fuel	Height	m	0.065
	Dry fuel density	$\mathrm{kg\,m^{-3}}$	511
	Surface area-to-volume ratio	$\mathrm{m^{-1}}$	3057
	Packing ratio	-	0.035
	Pre-exponential factor (A_{pyr})	$\mathrm{s^{-1}}$	36300
	Activation energy (E_{pyr})	$\mathrm{Jmol^{-1}}$	60300
	Heat of combustion (ΔH_c)	$\mathrm{kJ\,kg^{-1}}$	16360
	Mass fraction of dry fuel converted to char	-	0.27
Moisture	Fuel moisture content (for constant FMC case only)	$\mathrm{m^{-1}}$	0.05
	Heat of vaporization of water$\left(\Delta H_{vap}\right)$	$\mathrm{kJ\,kg^{-1}}$	2259
	Pre-exponential factor (A_{H_2O})	$\mathrm{K^{1/2}\,s^{-1}}$	600,000
	Activation energy (E_{H_2O})	K	5800
Char	Density	$\mathrm{kg\,m^{-3}}$	511
	Thermal conductivity	$\mathrm{Wm^{-1}K^{-1}}$	0.11
	Specific heat (As a function of temperature T)	$\mathrm{kJ\,kg^{-1}K^{-1}}$	2.04
	Pre-exponential factor (A_{char})	$\mathrm{m\,s^{-1}}$	215
	Activation energy (E_{char})	K	9000
	Heat of formation (ΔH_{char})	$\mathrm{kJ\,kg^{-1}}$	-32740
	Mass fraction of char converted to ash	-	0.11
	Mass fraction of oxygen	-	1.65
Ash	Density	$\mathrm{kg\,m^{-3}}$	15
	Thermal conductivity	$\mathrm{Wm^{-1}K^{-1}}$	0.1
	Specific heat	$\mathrm{kJ\,kg^{-1}K^{-1}}$	2

Appendix E Parameters used to validate the fully coupled model in Validation Study 3

Table 5: Parameters used to perform the validation of the fully coupled model (based on Catchpole et al., 1998)

	Parameter	Unit	Value
Solid fuel	Height	m	0.203
	Dry fuel density	$\mathrm{kg\,m^{-3}}$	398
	Surface area-to-volume ratio	$\mathrm{m^{-1}}$	7596
	Packing ratio	-	0.005
	Pre-exponential factor (A_{pyr})	$\mathrm{s^{-1}}$	36300
	Activation energy (E_{pyr})	$\mathrm{Jmol^{-1}}$	60300
	Heat of combustion (ΔH_c)	$\mathrm{kJ\,kg^{-1}}$	17260
	Mass fraction of dry fuel converted to char	-	0.2
Moisture	Fuel moisture content (for constant FMC case only)	$\mathrm{m^{-1}}$	0.03, 0.055, 0.181
	Heat of vaporization of water$\left(\Delta H_{vap}\right)$	$\mathrm{kJ\,kg^{-1}}$	2259
	Pre-exponential factor (A_{H_2O})	$\mathrm{K^{1/2}\,s^{-1}}$	600,000
	Activation energy (E_{H_2O})	K	5800
Char	Density	$\mathrm{kg\,m^{-3}}$	398
	Thermal conductivity	$\mathrm{Wm^{-1}K^{-1}}$	0.11
	Specific heat (As a function of temperature T)	$\mathrm{kJ\,kg^{-1}K^{-1}}$	0.44 + 0.0008 T
	Pre-exponential factor (A_{char})	$\mathrm{m\,s^{-1}}$	430
	Activation energy (E_{char})	$\mathrm{Jmol^{-1}}$	74800
	Heat of formation (ΔH_{char})	$\mathrm{kJ\,kg^{-1}}$	-32370
	Mass fraction of char converted to ash	-	0.02
	Mass fraction of oxygen	-	1.65
Ash	Density	$\mathrm{kg\,m^{-3}}$	67
	Thermal conductivity	$\mathrm{Wm^{-1}K^{-1}}$	0.1
	Specific heat	$\mathrm{kJ\,kg^{-1}K^{-1}}$	2

Declaration of Interests

The authors declare no conflicts of interest.

Author Credit Statement

Ritambhara Raj Dubey: Model development, Formal analysis, Investigation, Methodology, Software, Validation, Writing – original draft, Writing – review & editing. **Neda Yaghoobian**: Conceptualization, Funding acquisition, Formal analysis, Investigation, Methodology, Supervision, Writing – original draft, Writing – review & editing.

Declaration of Funding

This work is supported by funding from the Department of Defense Strategic Environmental Research and Development Program (SERDP) grant number RC20-1298 and National Science Foundation (NSF) grant number CBET 2043103.

References

Alves, M., Batista, A., Soares, R., Ottaviano, M., & Marchetti, M. (2009). Fuel moisture sampling and modeling in Pinus elliottii Engelm. Plantations based on weather conditions in Paraná-Brazil. *iForest-Biogeosciences and Forestry*, *2*(3), 99.

Asensio, M. I., Cascón, J., Laiz, P., & Prieto-Herráez, D. (2023). Validating the effect of fuel moisture content by a multivalued operator in a simplified physical fire spread model. *Environmental Modelling & Software*, *164*, 105710.

Bardina, J., Ferziger, J., & Reynolds, W. (1980). Improved subgrid-scale models for large-eddy simulation. *13th Fluid and Plasmadynamics Conference*, 1357.

Borujerdi, P. R., Shotorban, B., Mahalingam, S., & Weise, D. R. (2019). Modeling of water evaporation from a shrinking moist biomass slab subject to heating: Arrhenius approach versus equilibrium approach. *International Journal of Heat and Mass Transfer*, *145*, 118672.

Burrows, N. (1999). Fire behaviour in jarrah forest fuels: 2. Field experiments. *CALMSCIENCE-COMO-*, *3*, 57–84.

Byram, G. M., Nelson, R. M., & others. (2015). An analysis of the drying process in forest fuel material. *General Technical Report-Southern Research Station, USDA Forest Service*, *SRS-200*.

Catchpole, E. A., Catchpole, W. R., N.R.Viney, McCaw, W. L., & Marsden-Smedley, J. B. (2001). Estimating fuel response time and predicting fuel moisture content from field data. *International Journal of Wildland Fire*, *10*(2), 215. https://doi.org/10.1071/WF01011

Catchpole, W., Catchpole, E., Butler, B., Rothermel, R., Morris, G., & Latham, D. (1998). Rate of spread of free-burning fires in woody fuels in a wind tunnel. *Combustion Science and Technology*, *131*(1–6), 1–37.

Chuvieco, E., Aguado, I., & Dimitrakopoulos, A. P. (2004). Conversion of fuel moisture content values to ignition potential for integrated fire danger assessment. *Canadian Journal of Forest Research*, *34*(11), 2284–2293.

Clements, C. B., Lareau, N. P., Seto, D., Contezac, J., Davis, B., Teske, C., Zajkowski, T. J., Hudak, A. T., Bright, B. C., Dickinson, M. B., & others. (2015). Fire weather conditions and fire–atmosphere interactions observed during low-intensity prescribed fires–RxCADRE 2012. *International Journal of Wildland Fire*, *25*(1), 90–101.

Coen, J. (2013). *Modeling wildland fires: A description of the Coupled Atmosphere-Wildland Fire Environment model (CAWFE)*.

Deardorff, J. W. (1980). Stratocumulus-capped mixed layers derived from a three-dimensional model. *Boundary-Layer Meteorology*, *18*, 495–527.

Dimitrakopoulos, A., Papaioannou, K. K., & others. (2001). Flammability assessment of Mediterranean forest fuels. *Fire Technology*, *37*(2), 143–152.

Diószegi, G., Immitzer, M., Müller, M. M., & Vacik, H. (2023). Effects of interaction between forest structure and precipitation event characteristics on fuel moisture conditions. *Agricultural and Forest Meteorology*, *342*, 109681.

Fan, J., Hu, T., Ren, J., Liu, Q., & Sun, L. (2023). A comparison of five models in predicting surface dead fine fuel moisture content of typical forests in Northeast China. *Frontiers in Forests and Global Change*, *6*, 1122087.

Ferguson, S. A., Ruthford, J. E., McKay, S. J., Wright, D., Wright, C., & Ottmar, R. (2002). Measuring moisture dynamics to predict fire severity in longleaf pine forests. *International Journal of Wildland Fire*, *11*(4), 267–279.

Ferguson, S. C., Dahale, A., Shotorban, B., Mahalingam, S., & Weise, D. R. (2013). The Role of Moisture on Combustion of Pyrolysis Gases in Wildland Fires. *Combustion Science and Technology*, *185*(3), 435–453. https://doi.org/10.1080/00102202.2012.726666

Fernandes, P. M., Botelho, H., Rego, F., & Loureiro, C. (2008). Using fuel and weather variables to predict the sustainability of surface fire spread in maritime pine stands. *Canadian Journal of Forest Research*, *38*(2), 190–201.

Filippi, J.-B., Bosseur, F., Mari, C., & Lac, C. (2018). Simulation of a Large Wildfire in a Coupled Fire-Atmosphere Model. *Atmosphere*, *9*(6), 218. https://doi.org/10.3390/atmos9060218

Finney, M., McAllister, S., Grumstrup, T., & Forthofer, J. (2021). *Wildland Fire Behaviour: Dynamics, Principles and Processes*. CSIRO Publishing. https://doi.org/10.1071/9781486309092

Forest, I., Station (Ogden, R. E., & Utah). (1984). *The 1978 national fire-danger rating system: Technical documentation* (Vol. 169). US Department of Agriculture, Forest Service, Intermountain Forest and Range ….

Grishin, A., Kuzin, A. Y., & Alekseenko, E. (2003). Determination of kinetic characteristics of the process of drying of forest combustibles. *Journal of Engineering Physics and Thermophysics*, *76*(5), 1160–1165.

Hiers, J. K., O'Brien, J. J., Varner, J. M., Butler, B. W., Dickinson, M., Furman, J., Gallagher, M., Godwin, D., Goodrick, S. L., Hood, S. M., Hudak, A., Kobziar, L. N., Linn, R., Loudermilk, E. L., McCaffrey, S., Robertson, K., Rowell, E. M., Skowronski, N., Watts, A. C., & Yedinak, K. M. (2020). Prescribed fire science: The case for a refined research agenda. *Fire Ecology*, *16*(1), 11, s42408-020-0070–0078. https://doi.org/10.1186/s42408-020-0070-8

Hou, X., Wu, Z., Zhu, S., Li, Z., & Li, S. (2024). Comparative Analysis of Machine Learning-Based Predictive Models for Fine Dead Fuel Moisture of Subtropical Forest in China. *Forests*, *15*(5), 736.

Iván, B., Juan, P., Luciana, A., Morales, J. M., & Thomas, K. (2023). Microclimate and species composition shape the contribution of fuel moisture to positive fire-vegetation feedbacks. *Agricultural and Forest Meteorology*, *330*, 109289.

Jonko, A. K., Yedinak, K. M., Conley, J. L., & Linn, R. R. (2021). Sensitivity of grass fires burning in marginal conditions to atmospheric turbulence. *Journal of Geophysical Research: Atmospheres*, *126*(13), e2020JD033384.

Kane, J. M. (2021). Stand conditions alter seasonal microclimate and dead fuel moisture in a Northwestern California oak woodland. *Agricultural and Forest Meteorology*, *308*, 108602.

Korobeinichev, O. P., Kumaran, S. M., Shanmugasundaram, D., Raghavan, V., Trubachev, S. A., Paletsky, A. A., Shmakov, A. G., Glaznev, R. K., Chernov, A. A., & Tereshchenko, A. G. (2022). Experimental and Numerical Study of Flame Spread Over Bed of Pine Needles. *Fire Technology*, *58*(3), 1227–1264. https://doi.org/10.1007/s10694-021-01190-2

Lenschow, D., Wyngaard, J. C., & Pennell, W. T. (1980). Mean-field and second-moment budgets in a baroclinic, convective boundary layer. *Journal of Atmospheric Sciences*, *37*(6), 1313–1326.

Letzel, M. O., Krane, M., & Raasch, S. (2008). High resolution urban large-eddy simulation studies from street canyon to neighbourhood scale. *Atmospheric Environment*, *42*(38), 8770–8784.

Lin, C.-C. (2004). Modeling fine dead fuel moisture in Taiwan red pine forests. 臺灣林業科學, *19*(1), 27–32.

Linn, R. R., Goodrick, S. L., Brambilla, S., Brown, M. J., Middleton, R. S., O'Brien, J. J., & Hiers, J. K. (2020). QUIC-fire: A fast-running simulation tool for prescribed fire planning. *Environmental Modelling & Software*, *125*, 104616.

Linn, R. R., Winterkamp, J. L., Furman, J. H., Williams, B., Hiers, J. K., Jonko, A., O'brien, J. J., Yedinak, K. M., & Goodrick, S. (2021). Modeling low intensity fires: Lessons learned from 2012 RxCADRE. *Atmosphere*, *12*(2), 139.

Linn, R., Reisner, J., Colman, J. J., & Winterkamp, J. (2002). Studying wildfire behavior using FIRETEC. *International Journal of Wildland Fire*, *11*(4), 233–246.

Loudermilk, E. L., Hiers, J. K., & O'Brien, J. J. (2017). The role of fuels for understanding fire behavior and fire effects. In *Ecological restoration and management of longleaf pine forests* (pp. 107–122). CRC Press.

Marcelli, T., Santoni, P. A., Simeoni, A., Leoni, E., & Porterie, B. (2004). Fire spread across pine needle fuel beds: Characterization of temperature and velocity distributions within the fire plume. *International Journal of Wildland Fire*, *13*(1), 37–48.

Marino, E., Yebra, M., Guillén-Climent, M., Algeet, N., Tomé, J. L., Madrigal, J., Guijarro, M., & Hernando, C. (2020). Investigating live fuel moisture content estimation in fire-prone shrubland from remote sensing using empirical modelling and RTM simulations. *Remote Sensing*, *12*(14), 2251.

Marshall, G. A., Linn, R. R., Holmes, M., Goodrick, S., Thompson, D. K., & Hemmati, A. (2023). Capturing sub-grid temperature and moisture variations for wildland fire modeling. *Environmental Modelling & Software*, *164*, 105678.

Martinuzzi, R., & Tropea, C. (1993). *The flow around surface-mounted, prismatic obstacles placed in a fully developed channel flow (data bank contribution)*.

Matthews, S. (2006). A process-based model of fine fuel moisture. *International Journal of Wildland Fire*, *15*(2), 155–168.

Matthews, S. (2014). Dead fuel moisture research: 1991–2012. *International Journal of Wildland Fire*, *23*(1), 78. https://doi.org/10.1071/WF13005

McCaw, W. L. (1997). *Predicting fire spread in Western Australian mallee-heath scrubland* [PhD Thesis]. University of New South Wales, Australian Defence Force Academy.

McDermott, R. J. (2005). *Toward one-dimensional turbulence subgrid closure for large-eddy simulation*. The University of Utah.

McGrattan, K. B., Baum, H. R., Rehm, R. G., Hamins, A., Forney, G. P., Floyd, J. E., Hostikka, S., & Prasad, K. (2004). Fire dynamics simulator (version 4) technical reference guide. *NIST Special Publication*, *1018*, 94.

Meerpoel-Pietri, K., Tihay-Felicelli, V., Graziani, A., Santoni, P.-A., Morandini, F., Perez-Ramirez, Y., Bosseur, F., Barboni, T., Sánchez-Monroy, X., & Mell, W. (2022). Modeling with WFDS Combustion Dynamics of Ornamental Vegetation Structures at WUI: Focus on the Burning of a Hedge at Laboratory Scale. *Combustion Science and Technology*, 1–31. https://doi.org/10.1080/00102202.2021.2019235

Meinders, E. R. (1998). *Experimental study of heat transfer in turbulent flows over wall-mounted cubes*.

Mell, W., Charney, J., Jenkins, M. A., Cheney, P., & Gould, J. (2013). Numerical Simulations of Grassland Fire Behavior from the LANL-FIRETEC and NIST-WFDS Models. In J. J. Qu, W. T. Sommers, R. Yang, & A. R. Riebau (Eds.), *Remote Sensing and Modeling*

Applications to Wildland Fires (pp. 209–225). Springer Berlin Heidelberg. https://doi.org/10.1007/978-3-642-32530-4_15

Mell, W., Jenkins, M. A., Gould, J., & Cheney, P. (2007). A physics-based approach to modelling grassland fires. *International Journal of Wildland Fire*, *16*(1), 1–22.

Miller, L., Zhu, L., Yebra, M., Rüdiger, C., & Webb, G. I. (2023). Projecting live fuel moisture content via deep learning. *International Journal of Wildland Fire*, *32*(5), 709–727.

Morvan, D. (2011). Physical phenomena and length scales governing the behaviour of wildfires: A case for physical modelling. *Fire Technology*, *47*(2), 437–460.

Morvan, D. (2013). Numerical study of the effect of fuel moisture content (FMC) upon the propagation of a surface fire on a flat terrain. *Fire Safety Journal*, *58*, 121–131.

Nelson Jr, R. M. (1984). A method for describing equilibrium moisture content of forest fuels. *Canadian Journal of Forest Research*, *14*(4), 597–600.

Nelson Jr, R. M. (2001). Water relations of forest fuels. In *Forest fires* (pp. 79–149). Elsevier.

Noble, I., Gill, A., & Bary, G. (1980). McArthur's fire-danger meters expressed as equations. *Australian Journal of Ecology*, *5*(2), 201–203.

Parsons, R. A., Linn, R. R., Pimont, F., Hoffman, C., Sauer, J., Winterkamp, J., Sieg, C. H., & Jolly, W. M. (2017). Numerical investigation of aggregated fuel spatial pattern impacts on fire behavior. *Land*, *6*(2), 43.

Perez-Ramirez, Y., Mell, W. E., Santoni, P. A., Tramoni, J. B., & Bosseur, F. (2017). Examination of WFDS in Modeling Spreading Fires in a Furniture Calorimeter. *Fire Technology*, *53*(5), 1795–1832. https://doi.org/10.1007/s10694-017-0657-z

Perez-Ramirez, Y., Santoni, P.-A., Tramoni, J., & Mell, W. (2014). Numerical simulations of spreading fires in a large-scale calorimeter: The influence of the experimental configuration. *Proceedings of the VII International Conference on Forest Fires Research*.

Pimont, F., Parsons, R., Rigolot, E., de Coligny, F., Dupuy, J.-L., Dreyfus, P., & Linn, R. R. (2016). Modeling fuels and fire effects in 3D: model description and applications. *Environmental Modelling & Software*, *80*, 225–244.

Pimont, F., Ruffault, J., Martin-StPaul, N., & Dupuy, J.-L. (2019). Why is the effect of live fuel moisture content on fire rate of spread underestimated in field experiments in shrublands? *International Journal of Wildland Fire*, *28*(2), 127–137.

Potter, B. E. (2005). The role of released moisture in the atmospheric dynamics associated with wildland fires. *International Journal of Wildland Fire*, *14*(1), 77–84.

Quan, X., He, B., Jaafari, A., Liao, Z., Liu, X., Yue, C., & Chen, R. (2024). An overview of remotely sensed fuel variables for the prediction of wildf ires. *Remote Sensing of Soil and Land Surface Processes*, 407–417.

Raasch, S., & Etling, D. (1991). Numerical simulation of rotating turbulent thermal convection. *Contributions to Atmospheric Physics*, *64*(3), 185–199.

Rao, K., Williams, A. P., Flefil, J. F., & Konings, A. G. (2020). SAR-enhanced mapping of live fuel moisture content. *Remote Sensing of Environment*, *245*, 111797.

Ray, D., Nepstad, D., & Brando, P. (2010). Predicting moisture dynamics of fine understory fuels in a moist tropical rainforest system: Results of a pilot study undertaken to identify proxy variables useful for rating fire danger. *New Phytologist*, *187*(3), 720–732.

Robertson, K. M., Hsieh, Y. P., & Bugna, G. C. (2014). Fire environment effects on particulate matter emission factors in southeastern US pine-grasslands. *Atmospheric Environment*, *99*, 104–111.

Rodi, W. (1997). Comparison of LES and RANS calculations of the flow around bluff bodies. *Journal of Wind Engineering and Industrial Aerodynamics*, *69*, 55–75.

Rothermel, R. C. (1972). *A mathematical model for predicting fire spread in wildland fuels* (Vol. 115). Intermountain Forest & Range Experiment Station, Forest Service, US ….

Sharples, J. J., McRae, R. H., Weber, R., & Gill, A. M. (2009). A simple index for assessing fuel moisture content. *Environmental Modelling & Software*, *24*(5), 637–646.

Simms, D., & Law, M. (1967). The ignition of wet and dry wood by radiation. *Combustion and Flame*, *11*(5), 377–388.

Skamarock, W. C., & Klemp, J. B. (2008). A time-split nonhydrostatic atmospheric model for weather research and forecasting applications. *Journal of Computational Physics*, *227*(7), 3465–3485.

Stocks, B. J., Lawson, B., Alexander, M., Wagner, C. V., McAlpine, R., Lynham, T., & Dube, D. (1989). The Canadian forest fire danger rating system: An overview. *The Forestry Chronicle*, *65*(6), 450–457.

Tanskanen, H., Granström, A., Venäläinen, A., & Puttonen, P. (2006). Moisture dynamics of moss-dominated surface fuel in relation to the structure of Picea abies and Pinus sylvestris stands. *Forest Ecology and Management*, *226*(1–3), 189–198.

Tseng, Y.-H., Meneveau, C., & Parlange, M. B. (2006). Modeling flow around bluff bodies and predicting urban dispersion using large eddy simulation. *Environmental Science & Technology*, *40*(8), 2653–2662.

Vinodkumar, V., Dharssi, I., Yebra, M., & Fox-Hughes, P. (2021). Continental-scale prediction of live fuel moisture content using soil moisture information. *Agricultural and Forest Meteorology*, *307*, 108503.

Wiesner, S., Staudhammer, C. L., Javaheri, C. L., Hiers, J. K., Boring, L. R., Mitchell, R. J., & Starr, G. (2019). The role of understory phenology and productivity in the carbon dynamics of longleaf pine savannas. *Ecosphere*, *10*(4). https://doi.org/10.1002/ecs2.2675

Willis, G., & Deardorff, J. (1974). A laboratory model of the unstable planetary boundary layer. *Journal of Atmospheric Sciences*, *31*(5), 1297–1307.

Wittich, K.-P. (2005). A single-layer litter-moisture model for estimating forest-fire danger. *Meteorologische Zeitschrift*, 157–164.

Wu, Z., He, H. S., Fang, L., Liang, Y., & Parsons, R. A. (2018). Wind speed and relative humidity influence spatial patterns of burn severity in boreal forests of northeastern China. *Annals of Forest Science*, *75*, 1–13.

Yebra, M., Dennison, P. E., Chuvieco, E., Riaño, D., Zylstra, P., Hunt Jr, E. R., Danson, F. M., Qi, Y., & Jurdao, S. (2013). A global review of remote sensing of live fuel moisture content for fire danger assessment: Moving towards operational products. *Remote Sensing of Environment*, *136*, 455–468.

Zhao, N., Li, B., Ahmad, R., Ding, F., Zhou, Y., Li, G., Zayan, A. M. I., & Dong, R. (2021). Dynamic relationships between real-time fuel moisture content and combustion-emission-performance characteristics of wood pellets in a top-lit updraft cookstove. *Case Studies in Thermal Engineering*, *28*, 101484.